Journal of the Taiwan Institute of Chemical Engineers 189 (2026) 106869

Contents lists available at ScienceDirect

Journal of the Taiwan Institute of Chemical Engineers

journal homepage: www.journals.elsevier.com/journal-of-the-taiwan-institute-of-chemical-engineers

High-performance triboelectric nanogenerator based on luffa-derived cellulosic porous membrane for sustainable energy harvesting

Dinh Nam Nguyen [a], Ting-Han Lin [b], Ha Thi Vu Nguyen [a], Ming-Chung Wu [b,c,d], Nguyen Xuan Duong [e], Duy Linh Vu [a,*]

[a] Faculty of Materials Science and Engineering, Phenikaa School of Engineering, Phenikaa University, Hanoi 12116, Vietnam
[b] Center for Sustainability and Energy Technologies, Chang Gung University, Taoyuan 333323, Taiwan
[c] Department of Chemical and Materials Engineering, College of Engineering, Chang Gung University, Taoyuan 333323, Taiwan
[d] Division of Neonatology, Department of Pediatrics, Chang Gung Memorial Hospital, Linkou, Taoyuan 333423, Taiwan
[e] Faculty of Electronics and Telecommunications, VNU University of Engineering and Technology, Vietnam National University, Hanoi 12116, Vietnam.

ARTICLE INFO

Keywords:
Luffa-derived cellulosic
Bio-based material
Renewable energy
Triboelectric nanogenerator
Sustainability

ABSTRACT

Background: The exploration of eco-friendly and renewable materials for energy harvesting has attracted immense attention in recent years. Among these available materials, cellulose is particularly attractive due to its natural abundance, excellent biocompatibility, and inherent surface polarity.
Methods: We report a high-performance triboelectric nanogenerator (TENG) based on a luffa-derived cellulosic porous (LCP) membrane, fabricated without any inorganic coatings or synthetic modifications. This work systematically exploits the intrinsic three-dimensional porous architecture and hydroxyl-rich surface chemistry of LCP to enable humidity-assisted proton transport and Schottky-junction-regulated direct-current output without external rectification. The hierarchically porous structure of luffa provides a high specific surface area and excellent water absorption capacity, enabling efficient charge transfer through interfacial contact and hydrogen-bond-assisted proton transport.
Significant findings: The LCP-TENG delivers the optimal current of 1145.6 μA, a voltage of 0.57 V, and a power density of 19.1 μW/cm^2. The LCP-TENG demonstrates remarkable stability over 10,000 operation cycles even under high-humidity conditions. The harvested energy is sufficient to power a digital hygrometer, highlighting the device's potential for wearable electronics and sustainable energy applications. Overall, this study demonstrates a scalable and eco-friendly strategy for developing high-efficiency, bio-based triboelectric materials for next-generation green electronic systems.

1. Introduction

The accelerating developments of portable and wearable electronics, including smart watches, electronic skins, and environmental sensing, have accelerated the demand for lightweight, flexible, and environmentally sustainable power supplies [1–3]. Although electrochemical batteries remain the dominant energy storage solution, their limited service life, risk of leakage, and environmental toxicity raise concerns over long-term sustainability. Moreover, the frequent replacement or recharging of batteries limits the practical deployment of autonomous sensor systems, especially in remote or harsh environments [4–7]. Consequently, there is growing interest in alternative energy-harvesting strategies capable of capturing abundant ambient energy and directly converting it into electrical output, among which piezoelectric nanogenerators have been widely explored based on deformation-induced polarization changes. However, their performance often relies on piezoelectric fillers, poling treatment, or complex composite designs [8–10]. In this context, triboelectric nanogenerators (TENGs), represent a revolutionary approach for mechanical-to-electrical energy by coupling contact electrification with electrostatic induction [11–14]. Owing to their simple device structure, low fabrication cost, scalability, and broad material compatibility, TENGs particularly attractive for harvesting low-frequency mechanical energy from human motion [15], vibration [16], wind [17,18], water waves [19,20].

Direct-current TENGs (DC-TENGs) have recently emerged as an advanced extension of conventional alternating-current TENGs, owing

* Corresponding author.
E-mail address: linh.vuduy@phenikaa-uni.edu.vn (D.L. Vu).

https://doi.org/10.1016/j.jtice.2026.106869
Received 24 February 2026; Received in revised form 5 May 2026; Accepted 5 June 2026
Available online 10 June 2026

to their capability to generate continuous unidirectional electrical output without relying on external rectification circuits. This DC output minimizes energy losses, simplifies circuit design, and reduces power management demands, thereby markedly improving the overall energy conversion efficiency of TENG systems [21–24]. To realize direct-current operation, several approaches including Schottky junction modulation, tribovoltaic mechanisms, and asymmetric charge-transport interfaces have been developed, achieving significant enhancements in output current and power density [25–28]. By suppressing charge backflow and enabling directional carrier transport, DC-TENG architecture offer an effective route to overcome the intrinsic performance limitations of conventional TENGs, thus advancing high-efficiency mechanical energy harvesting and dependable self-powered electronic systems. Nevertheless, the operational stability of DC-TENGs remains challenged under harsh conditions such as high humidity and direct fluid exposure.

Achieving reliable TENG performance under moisture-rich conditions necessitates the development of materials capable of maintaining high triboelectric charge densities in the presence of water. Beyond conventional surface passivation strategies, the intrinsic polarity of water molecules and their hydrogen-bonding capability can be exploited to facilitate interfacial charge transfer. Nevertheless, most high-performance TENGs reported to date rely on synthetic polymers such as polyvinylidene fluoride (PVDF) [29–31], polytetrafluoroethylene (PTFE) [32–34], and polydimethylsiloxane (PDMS) [16,35,36]. Although these polymers exhibit excellent triboelectric characteristics, they are intrinsically non-degradable and derived from petrochemical resources, raising serious concerns regarding microplastic pollution and long-term environmental sustainability [37–39]. In addition, their hydrophobic surfaces are highly susceptible to surface charge screening and interfacial instability under humid conditions, leading to rapid charge dissipation and pronounced performance degradation [11,25,27,40]. These limitations significantly restrict the reliable operation of TENGs in real-world, thereby motivating the development of sustainable and biodegradable alternatives that preserve high electrical output while enabling stable operation in moisture-rich conditions.

In recent years, natural polymers and biomass-derived materials, including chitosan, silk fibroin, and starch, have recently emerged as promising green triboelectric materials [41–44]. Among them, cellulose, the most abundant biopolymer on Earth, stands out due to its renewability, mechanical robustness, tunable surface chemistry, and intrinsic dipole alignment arising from β-1,4-glycosidic linkages along the polymer backbone [40,45]. The high density of hydroxyl groups on cellulose chains promotes strong hydrogen bonding and surface polarization, which are advantageous for effective triboelectric charge generation. Moreover, the inherent hydrophilicity of cellulose allows adsorption of ambient moisture, which enhances ionic conduction and proton mobility within the material [46,47]. This humidity-assisted charge transport mechanism renders cellulose-based TENGs intrinsically tolerant to environmental humidity, in sharp contrast to conventional hydrophobic polymer systems, highlighting cellulose as a highly attractive material for environmental moisture and high-performance triboelectric energy harvesting. Despite these advantages, many reported cellulose-based TENGs still rely on chemical functionalization, such as grafting functional groups, doping with conductive fillers, or depositing inorganic layers, to achieve competitive electrical output. Such treatments not only increase fabrication complexity but may also reduce biodegradability and sustainability. Consequently, the realization of a fully natural, modification-free cellulose-based TENG with high efficiency remains a critical challenge. In this regard, Luffa cylindrica, also known as sponge gourd or loofa, offers a unique and underexplored cellulose source [48,49]. Its chemical composition and physical structure vary with growth conditions and maturity, yet the naturally interconnected, microporous fibrous network, combined with low cost and environmental friendliness, has already enabled its use in energy storage [49–51]. Compared with conventional cellulose-based TENGs that commonly use cellulose papers, or cellulose sponge as triboelectric layers, luffa-derived cellulose retains a native three-dimensional porous framework inherited from the biomass precursor. This hierarchical architecture provides a larger effective contact area, faster water uptake, and continuous moisture-assisted transport pathways. This hierarchical architecture provides a larger effective contact area, faster water uptake, and continuous moisture-assisted transport pathways. These intrinsic structural features suggest that luffa-derived cellulose is highly suited for triboelectric energy harvesting. However, comprehensive studies on luffa-derived cellulose for triboelectric energy harvesting are still limited.

In this work, we present a high-performance TENG based on a luffa-derived cellulosic porous (LCP) membrane, fabricated without the use of inorganic coatings or synthetic polymer modifications. The naturally formed porous microchannel structure of luffa cellulose provides a large effective surface area and strong water absorption capability, enabling intimate interfacial contact and facilitating hydrogen-bond-assisted proton transport during triboelectric operation. Owing to these structural, the LCP-TENG exhibits enhanced electrical output with stable current and power generation. Importantly, the device maintains stable electrical performance over 10,000 operation cycles even under high-humidity conditions, highlighting its robustness in moisture-rich environments, where conventional polymer-based TENGs experience pronounced degradation. These results show the LCP membrane as a scalable, environmentally benign, and efficient triboelectric material, offering a promising pathway toward next-generation green electronics.

2. Experimental section

2.1. Fabrication of luffa-derived cellulosic porous membrane

The luffa-derived cellulosic membrane was fabricated through chemical purification and thermal pressing process, as illustrated in Fig. 1a. Raw *luffa cylindrica* was purchased from a local supplier, rinsed with deionized water to remove surface dust, and cut into small pieces. The cleaned samples were treated in 10.0 wt% NaOH solution at 90 °C for 2 h to remove lignin and hemicellulose components. After alkaline treatment, the *luffa cylindrica* repeatedly washed with deionized water until a neutral pH was achieved, followed by a bleaching step using a 5.0 wt% hydrogen peroxide solution at 80 °C for 1 h. The purified luffa cellulose sponge was washed and dried at 60 °C for 12 h. Subsequently, the luffa cellulose sponge was mechanically pressed into a thin sheet and hot-pressed at 80 °C under a pressure of 5.0 MPa for 10 minutes to form luffa-derived cellulosic porous (LCP) membrane. Prior to device assembly, the membrane was stored in a desiccator to prevent uncontrolled moisture adsorption. *2.2 Fabrication of LCP-TENG device*: The TENG device was assembled by attaching the LCP membrane to an aluminum (Al) tape, which served as the top electrode. For the counter electrode, a copper (Cu) tape was attached to substrate to function as the bottom electrode (Fig. 1a).

2.2. Characterization and measurements

Morphological analysis of the LCP membrane was performed using field-mission scanning electron microscopy (FE-SEM, Hitachi S4800) to observe fiber arrangement and porosity. Chemical composition was verified by Fourier transform infrared spectroscopy (FTIR, Varian 640-IR) and X-ray diffraction (XRD, Bruker D8 Advance). Surface wettability was quantified through water contact angle measurements using an optical contact-angle goniometer. The output current and voltage of the TENG devices were recorded with a digital electrometer (DMM6500, Keithley)

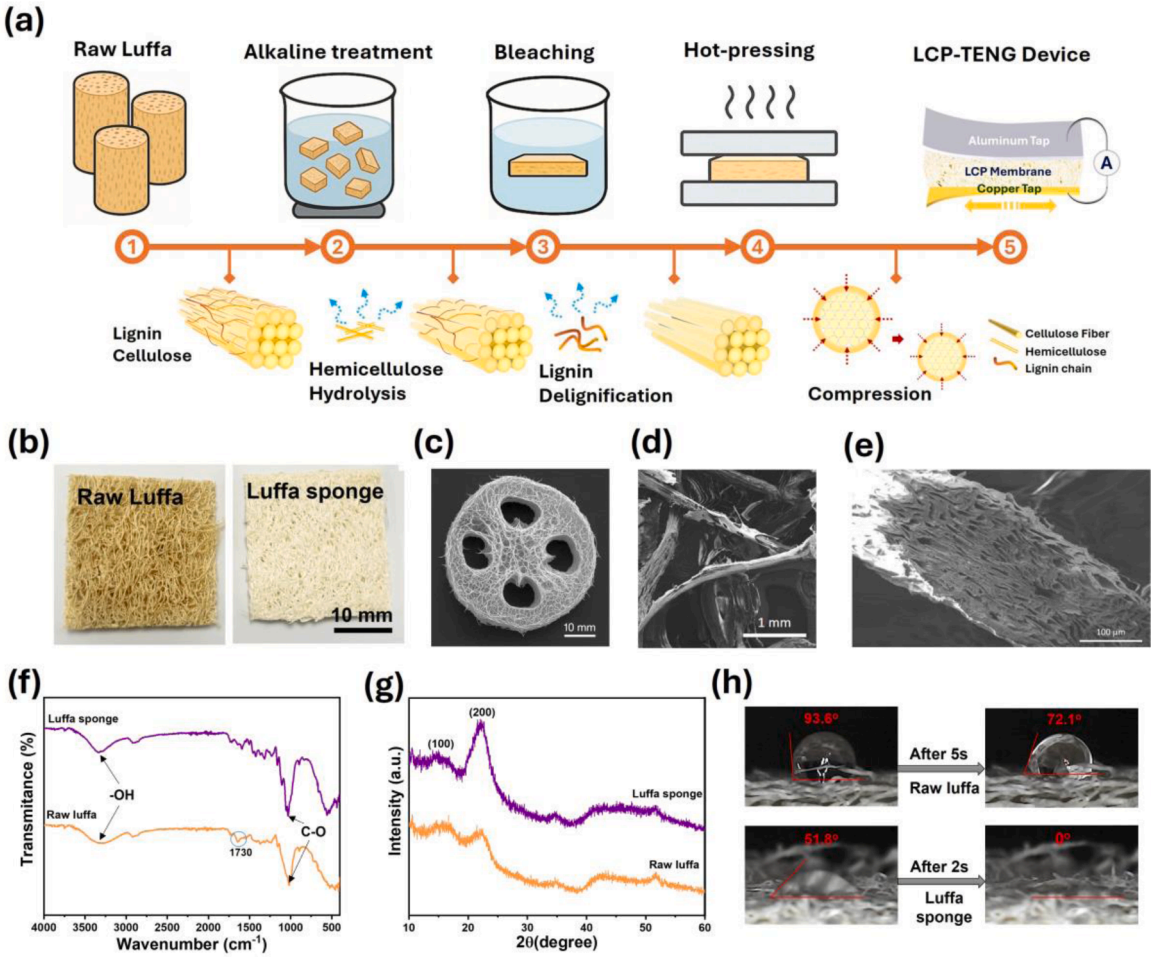

Fig. 1. **(a)** Schematic illustration of the fabrication process of the luffa-derived cellulosic porous (LCP) membrane and its integration into a triboelectric nanogenerator (TENG). The luffa precursor was subjected to sequential alkaline treatment and bleaching to remove hemicellulose and lignin. **(b)** Photographs of raw luffa and purified luffa sponge after chemical treatment. Morphological characterization of the LCP membrane: **(c)** cross-sectional view of the luffa sponge, **(d)** surface morphology, and **(e)** hierarchical microstructure of the luffa-derived cellulose fibers. Structural and surface analyses: **(f)** FTIR spectra, **(g)** XRD patterns, and **(h)** time-dependent water contact angle measurements of raw luffa and purified luffa sponge.

3. Results and discussion

3.1. Membrane characterization

High-purity luffa-derived cellulose was obtained through sequential chemical purification (Fig. 1a). Alkaline treatment selectively hydrolyzed hemicellulose, while subsequent bleaching effectively removed residual lignin, yielding a purified cellulose framework (Fig. 1b). After thermal compression to achieve a mechanically robust and homogeneous membrane, the luffa-derived cellulosic porous triboelectric nanogenerator (LCP-TENG) was assembled by laminating the membrane with aluminum and copper electrodes. SEM micrographs provide direct evidence of structural features of the resulting LCP membrane. LCP membrane exhibits an interconnected fibrous network forming a three-dimensional porous framework, indicative of high porosity and large specific surface area (Fig. 1c). High-magnification image resolve individual cellulose fibers are clearly observed with a ribbon-like morphology and rough surface texture (Fig. 1d), reflecting the exposure of bare cellulose fibers after chemical purification. A comparative analysis of structural evolution induced by purification was conducted (Supplementary **Fig. S1**). Raw luffa fibers exhibits dense and compact morphology with relatively smooth surfaces and larger apparent diameters. The presence of lignin, hemicellulose, and surface impurities binds the cellulose microfibrils into rigid bundles. Upon the alkaline treatment and bleaching, the non-cellulosic components are effectively removed, leading to thinner and more loosely packed, resulting in an open porous network. Cross-sectional SEM image further reveal a layered porous structure with continuous microchannels extending throughout the thickness (Fig. 1e). The preservation of abundant micro voids and folded lamellar features confirms that the intrinsic hierarchical porosity of luffa cellulose is well-retained after processing, facilitating high water uptake and efficient charge and proton transport in triboelectric application [52,53].

The FTIR and XRD analyses demonstrate that the sequential purification yields a cellulose-enriched framework while preserving the intrinsic crystal phase of native luffa. The FTIR spectrum of the LCP membrane retains the characteristic vibrations signatures of cellulose, including the broad O–H stretching band (3200-3500 cm^{-1}), C–H stretching (2890 cm^{-1}), and C–O stretching at ~1160–1030 cm^{-1}(Fig. 1f), indicating the preservation of the cellulose backbone after treatment. Notably, the carbonyl band at 1730 cm^{-1} associated with hemicellulose is suppresed after purification, providing direct spectroscopic evidence for the efficient removal of hemicellulose. Consistently, XRD patterns of both raw and purified sample exhibit the characteristic diffraction of cellulose I, with the dominant (200) reflection at $2\theta \approx 22–23^{\circ}$ and the lower-angle reflections in the 14–17° region (Fig. 1g), confirming the purification did not induce polymorphic transformation. The enhanced peak-to-background contrast observed in purified luffa sponge suggests an increase in relative crystallinity, which arised from the removal of amorphous lignin and hemicellulose establishes a

structurally consistent cellulose framework. This increase in cellulose-related diffraction intensity, together with the reduced amorphous background, further indicates that most amorphous non-cellulosic components were substantially removed during purification.

Beyond compositional and crystallographic changes, purification process induces a pronounced transition in surface wettability, as evidenced by the time-dependent contact-angle measurements (Fig. 1h and Supplementary **Video S1**). The raw luffa shows relatively hydrophobic behavior, with an initial contact angle of 93.6° that only decreases to 72.1° after 5.0 s, indicating limited wetting and slow water penetration. In contrast, the LCP membrane exhibits a substantially reduced initial contact angle (51.8°) and reaches complete wetting within 2.0 s, indicating rapid water spreading and continuous hydration throughout the porous network. Such rapid and continuous hydration is expected to establish a continuous water-assisted ionic/proton transport network, supporting the moisture-enabled charge transfer mechanism of the LCP-based triboelectric device.

3.2. *Working mechanism of LCP-TENG*

The LCP-TENG operates in a contact–separation mode, as illustrated in Fig. 2. Its output characteristics are primarily regulated by the Schottky junction formed at the interface between the LCP membrane and the Al electrode. In the initial configuration (Fig. 2a(i)), the two electrodes are physically separated, preventing effective charge exchange. The hydrogen-bonded network within the LCP originates from the abundant hydroxyl groups of cellulose, which can form extensive intra- and intermolecular hydrogen bonds in the cellulose I structure [45–47]. In the initial state, this network remains electrically neutral (Fig. 2b(i)), and the external circuit stays in an open-circuit state. When an external force brings the LCP membrane into contact with the Al electrode (Fig. 2a(ii)), the mismatch in work functions drives interfacial charge separation, inducing electron flow from the Al electrode toward the Cu electrode. Simultaneously, a Schottky barrier accompanied by the formation of a depletion region develops at the LCP–Al interface (Fig. 2b(ii)). With continued mechanical deformation (Fig. 2a(iii)) the friction energy excites charge carriers to higher energy states. Driven by the built-in electric field across the Schottky junction, the excited electrons overcome the interfacial barrier and migrate toward the Al electrode (Fig. 2b(iii)). This asymmetric carrier transport establishes a unidirectional electron flow through the external circuit, generating a direct-current output. An equivalent circuit model of the LCP-TENG is provided in Supplementary **Fig. S2**.

To elucidate the crucial role of hydration on device performance, we compared the electrical outputs of the LCP-TENG under dry and wet conditions (Fig. 3a-c). Here, the wet condition refers to the hydrated state of the LCP membrane after water absorption. To prepare the wet-state LCP membrane, the membrane was immersed in deionized water to allow sufficient water uptake, and the excess surface water was gently removed before electrical measurement. Upon hydration, the LCP-TENG generates a current of 469.5 μA, which is two orders higher than dry-state current of 2.7 μA. In contrast, the output voltage decreases after hydration, which can be attributed to proton-exchange–induced resistive losses in the composite membrane. Hydration introduces mobile ions/protons that lower the internal resistance of the device and thereby reduce the measured voltage. These mobile ions/protons mainly originate from absorbed water molecules interacting with the hydroxyl-rich cellulose framework, where proton exchange and proton hopping can occur along the cellulose–water hydrogen-bonded network [11,54]. Moreover, the power characteristics also exhibit a pronounced hydration-state-dependent shift in low load resistance (Fig. 3c). In the wet state, a peak power density of 18.4 μW is achieved at a low external load of 220 Ω, approximately 12 times larger than the dry-state maximum (1.5 μW) which appears only at a much higher load resistance (20 MΩ). This substantial shift of the output power density toward lower load resistance under wet conditions is consistent with a significant reduction in the internal resistance of device. Mechanistically, moisture absorption promotes the formation of hydrogen-bonded water networks (Fig. 3d) and hydrated protons accumulate near the interface of LCP membrane This interfacial proton enrichment lowers the

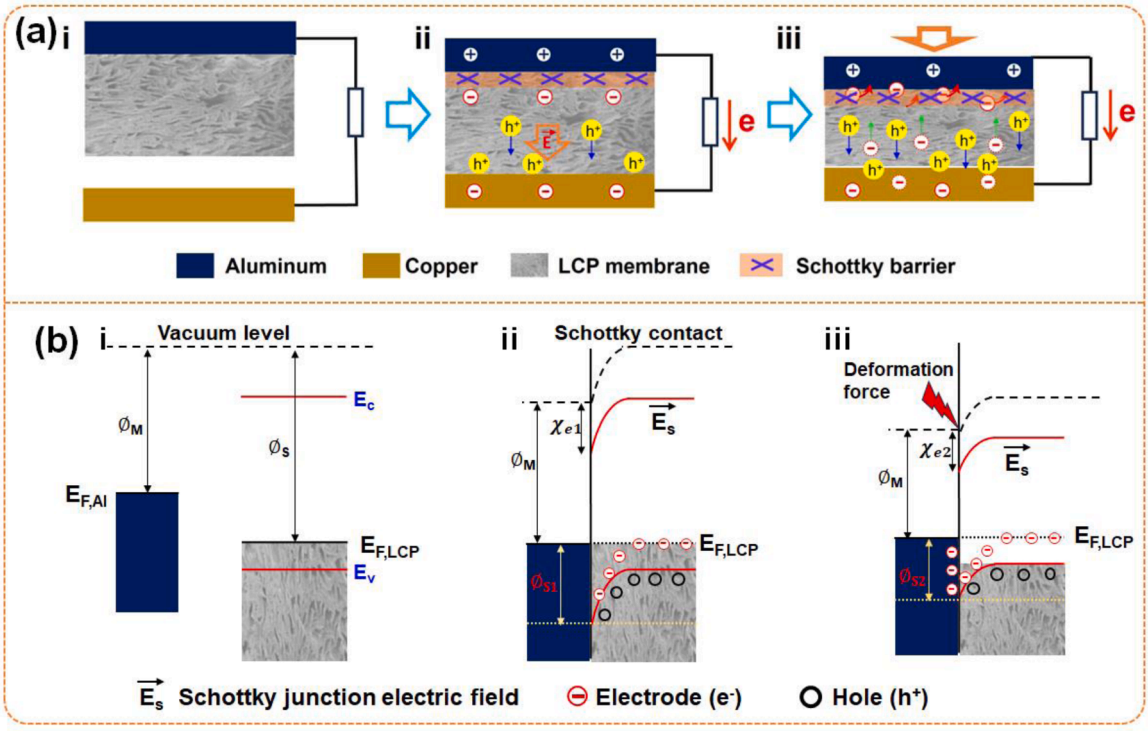

Fig. 2. **(a)** Schematic illustration of the contact-separation working mechanism of the LCP-TENG. **(b)** Corresponding energy band diagrams of the LCP-Al Schottky junction under separation and contact states.

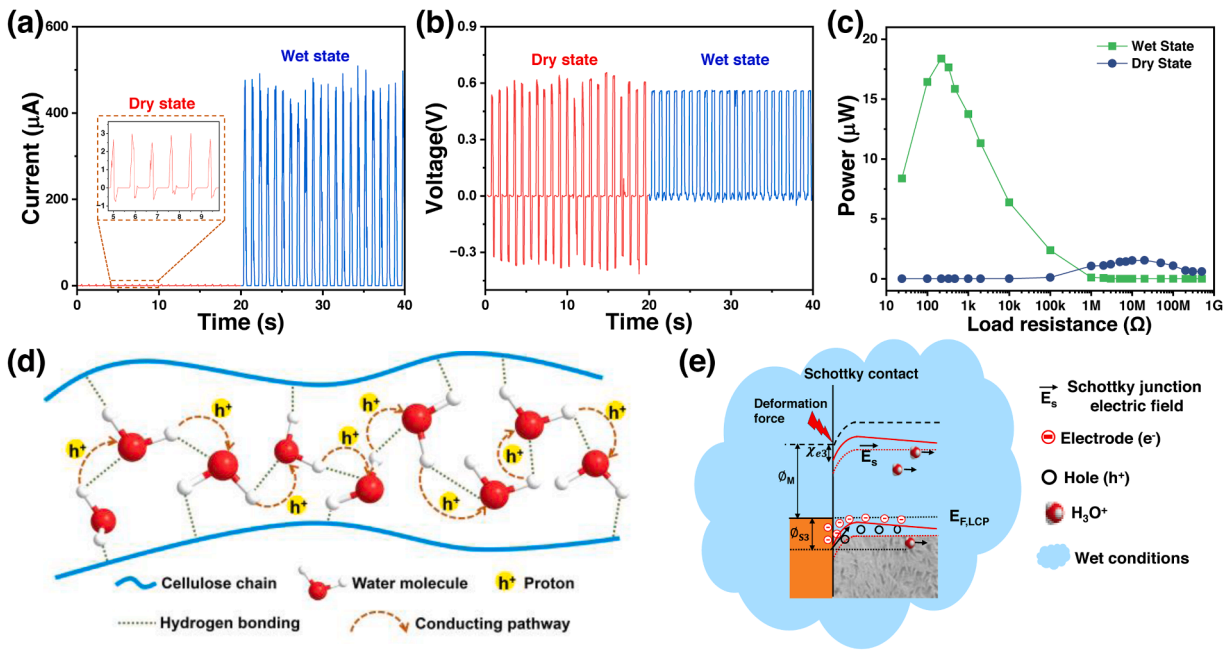

Fig. 3. **(a)** Current, **(b)** voltage, and **(c)** power density as a function of external load resistance for the LCP-TENG in dry and wet states. **(d)** Schematic illustration of the charge-transport pathways inside the LCP membrane. **(e)** Proposed working mechanism of the LCP-TENG under wet conditions.

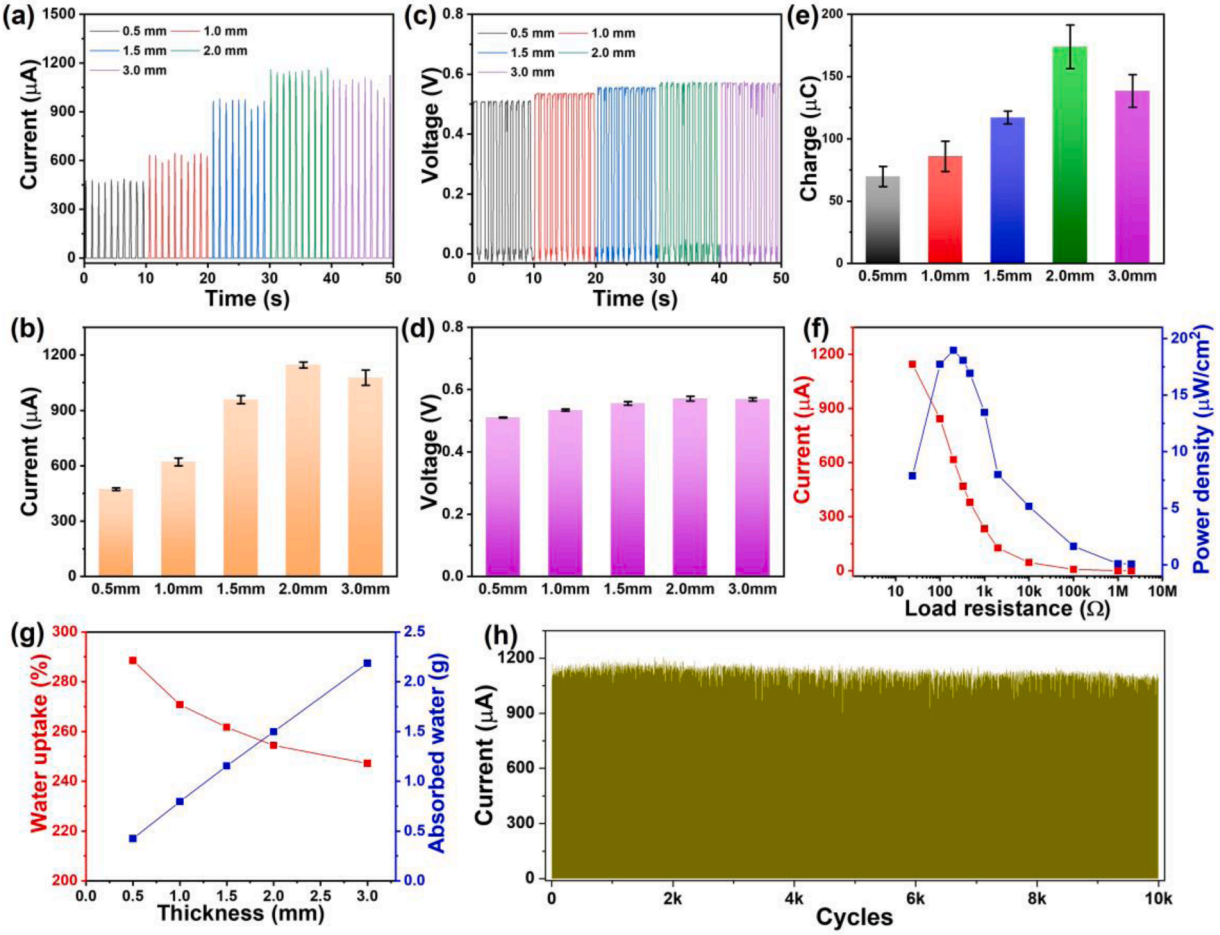

Fig. 4. (**a**) Output current and (**b**) comparative current plots; (**c**) output voltage and (**d**) comparative voltage plots; (**e**) transferred charge of LCP-TENGs with different LCP membrane thicknesses; (**f**) current and power density as a function of external load for the 2.0 mm LCP-TENG; (**g**) water uptake and absorbed water of the LCP membrane (2.0 mm); and (**h**) operational stability of the LCP-TENG over 10,000 cycles.

Schottky barrier at LCP-Al junction, facilitating electron injection into the electrode. To verify that Schottky contact is retained, the current–voltage (I-V) response of the Al/LCP/Cu was measured, as shown in Supplementary **Fig. S3**. The I–V behavior is clearly moisture dependent: under dry conditions the current remains nearly unchanged. After hydration, however, the device exhibits a distinct nonlinear, rectifying-like increase in current, consistent with Schottky-contact behavior where the interfacial barrier promotes preferential charge transport in a single direction and thus strengthens rectification [12]. In parallel, the increased ionic concentration enhances the internal electric field (E_s), which further facilitates effective charge separation (Fig. 3e). Collectively, the lowered Schottky barrier and increased charge density synergistically boost triboelectric charge generation and elevate the current output under humid conditions. Accordingly, the wet state LCP-TENG was selected for subsequent experiments and more detailed investigations.

3.3. Electrical performance and optimization

To ensure a reliable comparison of the electrical performance among different LCP membranes, all measurements in this section were conducted under fixed mechanical conditions. A custom-built mechanical actuator was used to operate the LCP-TENG in a vertical contact–separation mode. The device was tested in the wet state under an applied force of 10 N, an operating frequency of 1 Hz, and a deformation rate of 3 cm/s, thereby ensuring repeatable contact between the opposing layers. Fig. 4 summarizes the output characteristics of the LCP-TENG as a function of LCP membrane thickness. As the thickness increases from 0.5 to 2.0 mm, the current rises sharply, followed by a slight decline when the thickness is further increased to 3.0 mm (Fig. 4 (a,b)). The voltage shows a slight enhancement and generally follows the same thickness-dependent trend as the current (Fig. 4(c,d)). Notably, the LCP-TENG with a membrane thickness of 2.0 mm delivers the optimal performance, reaching 1145.6 μA and 0.57 V. These values are approximately 2.4-fold and 1.1-fold higher than those obtained with the 0.5 mm membrane, respectively. In addition, the transferred charge per single current peak was quantified by integrating the induced current signal, as depicted in Fig. 4e and Supplementary **Fig. S4.** The maximum transferred charge increases markedly with thickness, from 69.8 μC for the 0.5 mm membrane to 173.8 μC for the 2.0 mm membrane.

Fig. 4f shows how the output current and power density of the 2.0 mm LCP-TENG varies with the external load. When the load resistance increases from 24 Ω to 2 MΩ, the current decreases clearly, dropping from 1145.6 μA to 0.4 μA. The power density (P_d) was calculated using as follows:

$$P_d = \frac{P}{A} \tag{1}$$

where A is the effective contact area. As the load resistance increases, the power density initially rises to a maximum and subsequently declines at higher resistance. The highest power density, 19.1 μW/cm^2, is achieved at an optimal load of 220 Ω. Relative to previously reported mechanical energy-harvesting systems (Table 1), the LCP-TENG delivers a remarkably high output current of 1145.6 μA while maintaining a comparable power density, despite its relatively low output voltage. In addition, comparison with recent bio-based TENGs in **Table S1** shows that most biomass-derived systems mainly produce high voltage but relatively low current and often require chemical modification, composite formation, or functional fillers. By contrast, the present LCP-TENG relies only on the intrinsic porous structure and hydroxyl-rich surface of luffa-derived cellulose to enable humidity-assisted proton transport and direct-current output without external rectification. These advantages underscore the potential of the LCP-TENG as an inexpensive, scalable, and sustainable power source for practical self-powered electronics.

Table 1
Comparative evaluation of the output performance of Schottky-junction-based TENGs.

Active layer	Voltage (V)	Current (μA)	Power density (μW/cm^2)	Refs
Al/n-Si	0.6	4	0.525	[2]
MoS_2/AlN/Si	5.1	112	13	[55]
Al/PPy-coated fabric/Au	3.27	33	52	[56]
Cu/PVDF-IL/Al	1.36	1180	15.4	[54]
Al/PPy-TiO_2/Au	0.84	57	6.2	[26]
Al/Cellulose/Cu	0.5	2720	6.6	[25]
Cu/LCP/Al	0.57	1145.6	19.1	This work

Abbreviations: PPy, Polypyrrole; PVDF, polyvinylidene fluoride; IL, Ionic liquid.

The enhanced electrical output can also be attributed to charge exchange processes within the LCP membrane. As shown by the water-uptake and water-absorption results, (Fig. 4g), these hydration and transport related parameters generally increase with increasing membrane thickness. The 0.5 mm LCP membrane exhibits a water uptake of 288.5%, whereas the 3.0 mm sample shows a lower uptake of 247.2%. In contrast, the absolute water absorption rises substantially from 0.42 to 2.19 g, as the thickness increases from 0.5 to 3.0 mm. The larger volume of retained water promotes the formation of more extensive hydrogen-bonded networks, thereby facilitating more efficient charge transport through the LCP matrix and sustaining charge migration during operation, which leads to higher current output. Nevertheless, when the membrane becomes too thick (3.0 mm), the longer transport pathway and increased internal resistance begin to dominate. Charge transfer is then hindered, diminishing the advantages associated with high hydration, and the output consequently drops beyond the optimal thickness.

In addition, the long-term operational stability of the LCP-TENG was evaluated (Fig. 4h and Supplementary **Fig. S5)**. The device demonstrates outstanding durability, delivering nearly constant output over 10k working cycles. The current variation remains within 6%, which can be reasonably attributed to progressive mechanical abrasion and small changes in water content within the ionic/hydrogen-bonded network. Importantly, even after 30 days of storage under ambient conditions, the device still produces 1113.6 μA, corresponding to 97% retention of the initial output, indicating partial recovery of the output performance. This recovery is likely associated with relaxation of the compressed cellulose porous network and redistribution of water within the LCP membrane. Overall, these results indicate that the LCP-TENG offers robust mechanical stability and dependable performance, supporting its suitability for long-term practical energy-harvesting applications.

To optimize the electrical performance, we investigated the current output of the LCP-TENG under different applied forces. As presented in Fig. 5a, the peak current rises from 829.8 μA at 3 N to 1457.7 μA at 25 N, beyond which it tends to level off with further increases in force. This trend is primarily associated with load-driven interfacial compaction and membrane deformation, which effectively modulate the LCP-Al Schottky junction by reducing the effective barrier height, increasing carrier density near the junction, and lowering the charge-transport resistance within the LCP layer, in agreement with the mechanism discussed above. Meanwhile, increased mechanical loading strengthens contact electrification and frictional charge generation at the interface, further contributing to the enhanced current. Importantly, the current shows an approximately linear dependence on force within 5-25 N (Fig. 5b), with a sensitivity of 34.6 μA/N and strong fitting quality (R^2 = 0.908), highlighting the device's high force-responsiveness.

To elucidate the influence of membrane mobility on electrical output, we quantified the current response of the LCP-TENG as a function of absorbed water. As depicted in Fig. 5c, the peak current increased monotonically from 197.1 to 1145.6 μA when the water content rises

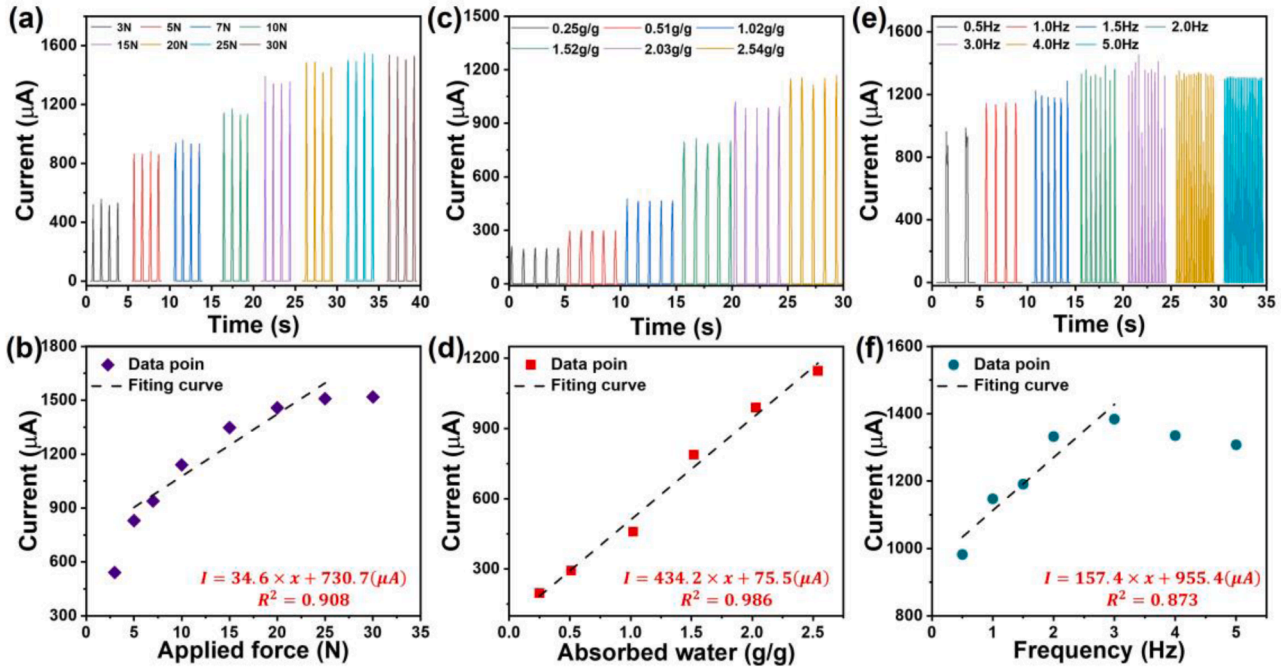

Fig. 5. Current output of the LCP-TENG measured as a function of **(a)** applied forces, **(c)** absorbed water in LCP membrane, and **(e)** frequency; corresponding electrical-response dependences on **(b)** applied forces, **(d)** absorbed water in LCP membrane, and **(f)** frequency.

from 0.25 to 2.54 g/g, approaching the saturated hydration regime. This pronounced enhancement originates from hydration-induced reinforcement of the water–cellulose hydrogen-bond network, which increases the mobility of charge carriers and facilitates more efficient charge migration through the LCP matrix, thereby amplifying the current output. A highly linear correlation is obtained over 0.25 – 2.54 g/g, delivering a sensitivity of 434.2 μA/(g/g) with an excellent linear fit (R^2-value=0.986) (Fig. 5d).

The device output also exhibits clear frequency-dependent behavior (Fig. 5e). Increasing the operating frequency from 0.5 to 3.0 Hz leads to a substantial rise in peak current from 983.1 to 1389.5 μA, consistent with accelerated contact electrification and enhanced charge pumping under faster mechanical cycling [57]. Beyond this regime, the current tends to saturate and slightly decrease, which can be attributed to incomplete contact–separation dynamics that limit full charge extraction, together with a reduced friction coefficient at higher relative velocities in wet interfaces that suppresses triboelectric charge generation [58]. Linear regression analysis further suggests an approximately linear

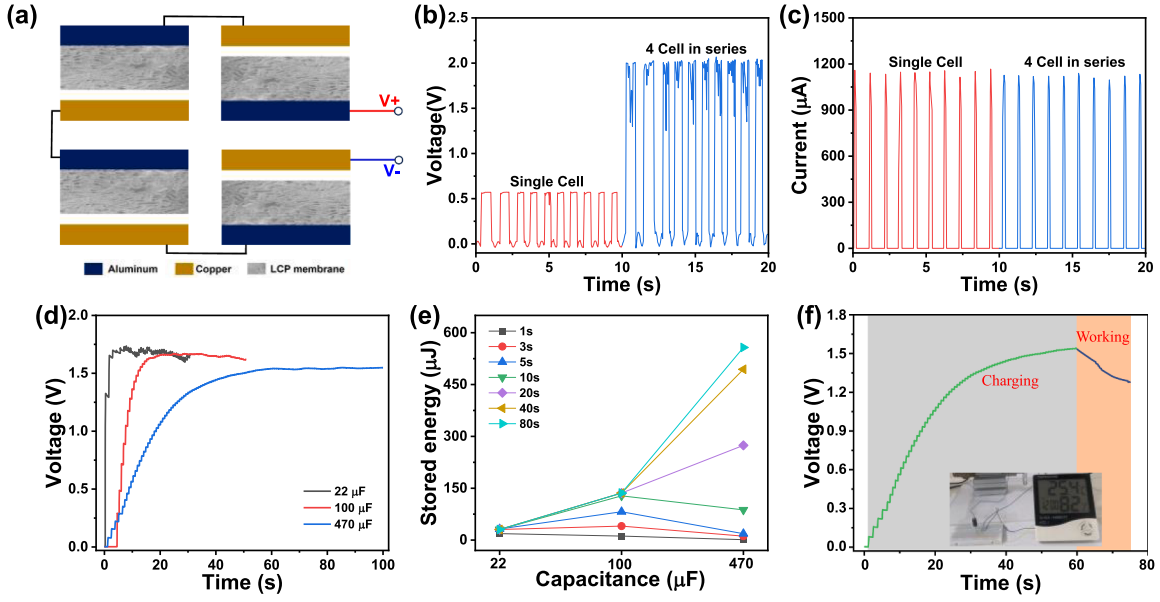

Fig. 6. **(a)** Illustration of a four-unit LCP-TENG series configuration. **(b)** Voltage and **(c)** current of a single LCP-TENG and four-unit series configuration. **(d)** Charging profiles of capacitors with different capacitances powered by LCP-TENG. **(e)** Stored energy obtained for capacitors with different capacitances. **(f)** Voltage–time profile of a 470 μF capacitor charged by the LCP-TENG while driving a commercial digital thermo-hygrometer (inset: photograph of the thermo-hygrometer in operation).

current–frequency relationship between 0.5 to 3.0 Hz, with a sensitivity of 434.2 μA/Hz (R^2= 0.87) (Fig. 5f).

3.4. Scaling up and application of LCP-TENG

Despite delivering a modest output voltage compared with the hundreds of volts typically reported for conventional TENGs [59–62], the LCP-TENG distinguishes itself by its markedly higher current and power density, which is advantageous for practical energy delivery. To overcome the voltage limitation and meet the threshold required by most electronic modules (≥1.5 V), multiple LCP-TENG units were integrated into series (Fig. 6a). As shown in Fig. 6b, the output voltage increases almost proportionally with the number of cells, rising from 0.57 for a single unit to 2.05 V for four units, which is sufficient for driving a range of low-power electronics, particularly those in IoT-oriented scenarios. In contrast, the output current remains nearly unchanged (Fig. 6c), because the same amount of transferred charge flows through each unit in a series string and the current is primarily constrained by the intrinsic impedance of individual unit in conjunction with the external load.

A key merit of the LCP-TENG lies in its direct-current output, enabling direct charging of energy-storage components without the need for rectification, thereby minimizing conversion losses. As illustrated in Fig. 6d, a 22 μF capacitor can be rapidly charged to 1.7 V within 3 s, while larger capacitor of 100 μF and 470 μF reach voltages of 1.6 and 1.5 V in 15 and 50 s, respectively. These results demonstrate efficient energy delivery across practically relevant range of capacitance. The corresponding evolution of stored energy as a function of capacitance and charging time is summarized in Fig. 6e. The stored energy (W_s) was calculated using:

$$W_s = \frac{1}{2}CV^2 \quad (2)$$

where C and V denote capacitance voltage, respectively. Notably, after 80 s of charging, the 470 μF capacitors stores approximately 557 μJ, sufficient to power several low-power electronic devices. To further validate the applicability, the harvested energy was used to operate a commercial digital thermo-hygrometer (HTC-1). After 40 s of charging, the stored energy sustained continuous operation for more than 20 s (Fig. 6f and Supplementary **Video S2)**. The corresponding charging and discharging profiles clearly demonstrate a stable energy supply, confirming the practical usability of system.

4. Conclusion

In conclusion, we report a sustainable and modification-free triboelectric nanogenerator enabled by a luffa-derived cellulosic porous (LCP) membrane. The inherent microchannel architecture and hydroxyl-rich cellulose framework synergistically promote interfacial charge generation and moisture-assisted charge transport for high-output energy harvesting. By optimizing the membrane thickness, the device delivers an outstanding current of 1145.6 μA and a voltage of 0.57 V an optimal thickness of 2.0 mm, together with a maximum power density of 19.1 μW/cm at a external load of 220 Ω. The LCP-TENG also exhibits robust durability, maintaining stable electrical performance over 10,000 mechanical cycles with minimal fluctuations and retaining 97% of the initial current after 30 days of ambient storage. For practical development, series integration of four LCP-TENG units increases the output voltage to 2.05 V without compromising current, enabling efficient direct capacitor charging and reliable operation of a commercial digital thermo-hygrometer without a need for rectification. Overall, this work establishes LCP membrane as a scalable, environmentally benign triboelectric material platform, and provides a viable strategy for high-current, durable mechanical energy harvesting and self-powered electronics, particularly in moisture-rich operating environments.

Data availability

Data will be made available on request.

CRediT authorship contribution statement

Dinh Nam Nguyen: Writing – original draft, Methodology, Investigation, Formal analysis, Data curation, Conceptualization. **Ting-Han Lin:** Writing – review & editing, Visualization, Conceptualization. **Ha Thi Vu Nguyen:** Investigation, Formal analysis, Data curation. **Ming-Chung Wu:** Writing – review & editing, Supervision. **Nguyen Xuan Duong:** Writing – review & editing, Investigation, Formal analysis. **Duy Linh Vu:** Writing – review & editing, Writing – original draft, Supervision, Project administration, Funding acquisition.

Declaration of competing interest

The authors declare that they have no known competing financial interests or personal relationships that could have appeared to influence the work reported in this paper.

Acknowledgements

This study was financially supported by Chang Gung University (URRPD2R0011, URRPD2Q0021, URRPD2Q0031 and URRPD2Q0041).

Supplementary materials

Supplementary material associated with this article can be found, in the online version, at doi:10.1016/j.jtice.2026.106869.

References

[1] Viswanathan P, Chandrasekhar A. Energizing geriatric healthcare: A triboelectric energy harvester with self-powered morse code generator and IoT-Enabled remote sensing tactile patch. Mater Today Sustain 2024;27:100801. https://doi.org/10.1016/j.mtsust.2024.100801.
[2] Lin S, Lu Y, Feng S, Hao Z, Yan Y. A High Current Density Direct-Current Generator Based on a Moving van der Waals Schottky Diode. Adv Mater 2019;31:1–7. https://doi.org/10.1002/adma.201804398.
[3] Gizaw DG, Periyasamy S, Beula Isabel J, Hunegnaw BM, Jayakumar M, Asaithambi P, et al. Potential oil sources, conversion routes and process limiting factors for sustainable biodiesel production – A comprehensive outlook. J Taiwan Inst Chem Eng 2025;177:106240. https://doi.org/10.1016/j.jtice.2025.106240.
[4] Raj A, Steingart D. Review—Power Sources for the Internet of Things. J Electrochem Soc 2018;165:B3130–6. https://doi.org/10.1149/2.0181808jes.
[5] Nguyen QT, Vu DL, Le CD, Ahn KK. Recent Progress in Self-Powered Sensors Based on Liquid-Solid Triboelectric Nanogenerators. Sensors 2023;23:5888. https://doi.org/10.3390/s2315888.
[6] Guo H, Zhao C. An Emerging Chemistry Revives Proton Batteries. Small Methods 2023;2300699:1–23. https://doi.org/10.1002/smtd.202300699.
[7] Livi S, Duchet-Rumeau J, Gérard J-F, Pham TN. Polymers and Ionic Liquids: A Successful Wedding. Macromol Chem Phys 2015;216:359–68. https://doi.org/10.1002/macp.201400425.
[8] Pereira N, Costa CM, Lanceros-Méndez S. Piezoelectric Smart and Multifunctional Materials. Adv. Smart Multifunct. Mater 2025;1:3–43. https://doi.org/10.1021/bk-2025-1513.ch003. Fundam. Types, vol. 1513, American Chemical Society.
[9] Damastuti R, Prasannan A, Yu H, Jayachitra R, Da Hong P. Fabrication of multifunctional perovskite PZT immobilized with PVDF-HFP as piezo-photocatalysts for energy production and environmental remediation. Surfaces and Interfaces 2025;60:106014. https://doi.org/10.1016/j.surfin.2025.106014.
[10] Luu-Dang D-T, Tran NM, Huynh HN-D, Nguyen T-A, Nguyen DQ, Yu W-Y, et al. Investigation of Al doped Rh@Cr2O3/SrTiO3 photocatalysts in overall seawater splitting with the synergetic electron mediators. J Taiwan Inst Chem Eng 2025;169:105971. https://doi.org/10.1016/j.jtice.2025.105971.
[11] Linh D, Tan Q, Seung P, Kwan K. Enhancing the charge transfer in triboelectric nanogenerator based on sulfonated poly ether ether ketone /carbon nanotubes proton exchange composite membrane. J Alloys Compd 2024;1004:175778. https://doi.org/10.1016/j.jallcom.2024.175778.
[12] Tan Q, Tam T, Van Linh D, Hwan J, Mook W, Kwan K. Ultrahigh current density DC triboelectric generator for energy harvesting and self-powered sensing. Nano Energy 2025;143:111291. https://doi.org/10.1016/j.nanoen.2025.111291.
[13] Wang ZL, Wang AC. On the origin of contact-electrification. Mater Today 2019;30:34–51. https://doi.org/10.1016/j.mattod.2019.05.016.
[14] Ke K-H, Lin L, Chung C-K. Low-cost micro-graphite doped polydimethylsiloxane composite film for enhancement of mechanical-to-electrical energy conversion

with aluminum and its application. J Taiwan Inst Chem Eng 2022;135:104388. https://doi.org/10.1016/j.jtice.2022.104388.
[15] Bai P, Zhu G, Lin ZH, Jing Q, Chen J, Zhang G, et al. Integrated multilayered triboelectric nanogenerator for harvesting biomechanical energy from human motions. ACS Nano 2013;7:3713–9. https://doi.org/10.1021/nn4007708.
[16] Ajimsha RS, Mahapatra A, Das AK, Sahu VK, Misra P. High output power density owing to enhanced charge transfer in ZnO-based triboelectric nanogenerator. Energy 2023;263:125646. https://doi.org/10.1016/j.energy.2022.125646.
[17] Liu X, Gao H, Sun L, Yao J. Generic Air-Gen Effect in Nanoporous Materials for Sustainable Energy Harvesting from Air Humidity. Adv Mater 2024;36:2300748. https://doi.org/10.1002/adma.202300748.
[18] Ellabban O, Abu-Rub H, Blaabjerg F. Renewable energy resources: Current status, future prospects and their enabling technology. Renew Sustain Energy Rev 2014; 39:748–64. https://doi.org/10.1016/j.rser.2014.07.113.
[19] Wang J, Wu Z, Pan L, Gao R, Zhang B, Yang L, et al. Direct-current rotary-tubular triboelectric nanogenerators based on liquid-dielectrics contact for sustainable energy harvesting and chemical composition analysis. ACS Nano 2019;13: 2587–98. https://doi.org/10.1021/acsnano.8b09642.
[20] Vu DL, Vo CP, Le CD, Ahn KK. Enhancing the output performance of fluid-based triboelectric nanogenerator by using poly(vinylidene fluoride-co-hexafluoropropylene)/ionic liquid nanoporous membrane. Int J Energy Res 2021; 45. https://doi.org/10.1002/er.6428.
[21] Luo J, Xu L, Tang W, Jiang T, Fan FR, Pang Y, et al. Direct-Current Triboelectric Nanogenerator Realized by Air Breakdown Induced Ionized Air Channel. Adv Energy Mater 2018;8:1–8. https://doi.org/10.1002/aenm.201800889.
[22] Chen S, Liu D, Zhou L, Li S, Zhao Z, Cui S, et al. Improved Output Performance of Direct-Current Triboelectric Nanogenerator through Field Enhancing Breakdown Effect. Adv Mater Technol 2021;6:1–7. https://doi.org/10.1002/admt.202100195.
[23] Han X, Niu J, Wang Y, Jin X, Peng L, Chen J, et al. Polyaniline-based Schottky-triboelectric hybrid DC generators with tunable electrical outputs. Nano Energy 2022;104:107956. https://doi.org/10.1016/j.nanoen.2022.107956.
[24] Vu DL, Lanh PT, Nguyen TT, Vu HAT, Nguyen QT, Nguyen VH, et al. High-Current Triboelectric Nanogenerator Based on TiO2-Decorated PVDF Membrane via Atomic Layer Deposition for Self-Powered Humidity Sensing. Small 2026:1–13. https://doi.org/10.1002/smll.202512870.
[25] Nguyen QT, Tran VT, Vu DL, Le CD, Choi WM, Ahn KK. Tribo-hygro-electric generator: Harnessing mechanical energy with liquid-infused porous cellulose for multiple sensing and DC power generation. Nano Energy 2024;132:110353. https://doi.org/10.1016/j.nanoen.2024.110353.
[26] Ding X, Shao H, Wang H, Yang W, Fang J, Zhang D, et al. Schottky DC generators with considerable enhanced power output and energy conversion efficiency based on polypyrrole-TiO2 nanocomposite. Nano Energy 2021;89:106367. https://doi.org/10.1016/j.nanoen.2021.106367.
[27] Chen J, He P, Huang T, Zhang D, Wang G, Yang S, et al. Boosting carrier transfer at flexible schottky junctions with moisture: A strategy for high-performance wearable direct-current nanogenerators. Nano Energy 2021;90:106593. https://doi.org/10.1016/j.nanoen.2021.106593.
[28] Xu X, Li J, Tao X, Yan Q, Wu H, Guan Z, et al. Study of interfacial design for direct-current tribovoltaic generators. Nano Energy 2022;94:106957. https://doi.org/10.1016/j.nanoen.2022.106957.
[29] Guo Y, Cao Y, Chen Z, Li R, Gong W, Yang W, et al. Fluorinated metal-organic framework as bifunctional filler toward highly improving output performance of triboelectric nanogenerators. Nano Energy 2020;70:104517. https://doi.org/10.1016/j.nanoen.2020.104517.
[30] Vu DL, Le CD, Ahn KK. Functionalized graphene oxide/polyvinylidene fluoride composite membrane acting as a triboelectric layer for hydropower energy harvesting. Int J Energy Res 2022;46. https://doi.org/10.1002/er.7824.
[31] Bhatta T, Maharjan P, Cho H, Park C, Yoon SH, Sharma S, et al. High-performance triboelectric nanogenerator based on MXene functionalized polyvinylidene fluoride composite nanofibers. Nano Energy 2021;81:105670. https://doi.org/10.1016/j.nanoen.2020.105670.
[32] Munirathinam K, Kim DS, Shanmugasundaram A, Park J, Jeong YJ, Lee DW. Flowing water-based tubular triboelectric nanogenerators for sustainable green energy harvesting. Nano Energy 2022;102:107675. https://doi.org/10.1016/j.nanoen.2022.107675.
[33] Kwak SS, Lin S, Lee JH, Ryu H, Kim TY, Zhong H, et al. Triboelectrification-Induced Large Electric Power Generation from a Single Moving Droplet on Graphene/Polytetrafluoroethylene. ACS Nano 2016;10:7297–302. https://doi.org/10.1021/acsnano.6b03032.
[34] Cheng G, Lin ZH, Du ZL, Wang ZL. Simultaneously harvesting electrostatic and mechanical energies from flowing water by a hybridized triboelectric nanogenerator. ACS Nano 2014;8:1932–9. https://doi.org/10.1021/nn406565k.
[35] Wen R, Guo J, Yu A, Zhai J, lin Wang Z. Humidity-Resistive Triboelectric Nanogenerator Fabricated Using Metal Organic Framework Composite. Adv Funct Mater 2019;29:1–9. https://doi.org/10.1002/adfm.201807655.
[36] Vafaiee M, Ejehi F, Mohammadpour R. OPEN CNT - PDMS foams as self - powered humidity sensors based on triboelectric nanogenerators driven by finger tapping. Sci Rep 2023:1–10. https://doi.org/10.1038/s41598-023-27690-5.
[37] Feng L, Wu Y, Qu J, Li Z, Wang J, Menon C. Advancing liquid-solid triboelectric nanogenerators via micro/nano-structured interface engineering. Compos Part B Eng 2026;309:113081. https://doi.org/10.1016/j.compositesb.2025.113081.
[38] Qu M, Shen L, Wang J, Zhang N, Pang Y, Wu Y, et al. Superhydrophobic, Humidity-Resistant, and Flexible Triboelectric Nanogenerators for Biomechanical Energy Harvesting and Wearable Self-Powered Sensing. ACS Appl Nano Mater 2022;5: 9840–51. https://doi.org/10.1021/acsanm.2c02026.
[39] Zhang J, Boyer C, Zhang YX. Enhancing the Humidity Resistance of Triboelectric Nanogenerators : A Review. Small 2024;2401846:1–18. https://doi.org/10.1002/smll.202401846.
[40] Rehman HMMU, Prasanna APS, Rehman MM, Khan M, Kim SJ, Kim WY. Edible rice paper-based multifunctional humidity sensor powered by triboelectricity. Sustain Mater Technol 2023;36:e00596. https://doi.org/10.1016/j.susmat.2023.e00596.
[41] Sardana S, Kaur H, Arora B, Aswal DK, Mahajan A. Self-Powered Monitoring of Ammonia Using an MXene/TiO2/Cellulose Nanofiber Heterojunction-Based Sensor Driven by an Electrospun Triboelectric Nanogenerator. ACS Sensors 2022;7: 312–21. https://doi.org/10.1021/acssensors.1c02388.
[42] Nguyen QT, Vu DL, Le CD, Ahn KK. Enhancing the Performance of Triboelectric Generator: A Novel Approach Using Solid–Liquid Interface-Treated Foam and Metal Contacts. Polymers (Basel) 2023;15. https://doi.org/10.3390/polym15102392.
[43] Yang L, Zhang L, Yong YC, Sun D. A Direct Current Self-Sustained Moisture-Electric Generator with 1D/2D Hierarchical Nanostructure for Continuous Operation of Off-Grid Electronics. ACS Nano 2024. https://doi.org/10.1021/acsnano.4c09494.
[44] He H, Zhang J, Pan J, Wang Z, Deng M, Liu X, et al. Moisture-Enabled Electric Generators Based on Electrospinning Silk Fibroin/Poly(ethylene oxide) Film Impregnated with Gradient-Structured Sericin. ACS Appl Energy Mater 2024;7: 2980–8. https://doi.org/10.1021/acsaem.4c00368.
[45] Nishiyama Y, Langan P, Chanzy H. Crystal Structure and Hydrogen-Bonding System in Cellulose Iβ from Synchrotron X-ray and Neutron Fiber Diffraction. J Am Chem Soc 2002;124:9074–82. https://doi.org/10.1021/ja0257319.
[46] Kovalenko VI. Crystalline cellulose: structure and hydrogen bonds. Russ Chem Rev 2010;79:231. https://doi.org/10.1070/RC2010v079n03ABEH004065.
[47] Wohlert M, Benselfelt T, Wa L, Berglund LA, Wohlert J. Cellulose and the role of hydrogen bonds : not in charge of everything 2022;4:1–23. https://doi.org/10.1007/s10570-021-04325-4.
[48] Akay O, Altinkok C, Acik G, Yuce H, Konuk G. A bio-based and non-toxic polyurethane film derived from Luffa cylindrica cellulose and ʟ -Lysine diisocyanate ethyl ester 2021;161:1–6.
[49] Li J, Ren Z, Ren Y, Zhao L, Wang S, Yu J. Activated carbon with micrometer-scale channels prepared from luffa sponge fibers and their application for supercapacitors. RSC Adv 2014;4:35789–96. https://doi.org/10.1039/C4RA04073B.
[50] Li S, Li W, Nie J, Liu D, Sui G. Synergistic effect of graphene nanoplate and carbonized loofah fi ber on the electromagnetic shielding effectiveness of PEEK-based composites. Carbon N Y 2019;143:154–61. https://doi.org/10.1016/j.carbon.2018.11.015.
[51] Tang W, Fu C, Xia L, Su L, Lyu P, Fu Z, et al. Biomass-derived multifunctional 3D film framed by carbonized loofah toward flexible strain sensors and triboelectric nanogenerators 2023;107. https://doi.org/10.1016/j.nanoen.2022.108129.
[52] Zhang K, Weng B, Cheng D, Guo Y, Chen T, Wang L, et al. Influence of chemical treatment and drying method on the properties of cellulose fibers of luffa sponge 2021;180:112–20. https://doi.org/10.1016/j.ijbiomac.2021.03.053.
[53] Jiang L, Ren Z, Chen S, Zhang Q, Lu X, Zhang H, et al. Bio-derived three-dimensional hierarchical carbon-graphene-TiO2 as electrode for supercapacitors. Sci Rep 2018;8:4412. https://doi.org/10.1038/s41598-018-22742-7.
[54] Linh D, Tan Q, Van Tam T, Mook W, Kwan K. Ionic liquids /poly (vinylidene fluoride) composite membrane for current boosting in direct-current triboelectric nanogenerator via Schottky junction. Nano Energy 2025;143:111322. https://doi.org/10.1016/j.nanoen.2025.111322.
[55] Lu Y, Hao Z, Feng S, Shen R, Yan Y, Lin S. Direct-Current Generator Based on Dynamic PN Junctions with the Designed Voltage Output. IScience 2019;22:58–69. https://doi.org/10.1016/j.isci.2019.11.004.
[56] Wang W, Han X, Niu J, Jin X, Wang H, Shao H, et al. Direct-current energy generators from polypyrrole-coated fabric/metal Schottky diodes with considerably improved output. J Mater Chem A 2020;8:24166–74. https://doi.org/10.1039/d0ta09342d.
[57] Shen X, Han W, Jiang Y, Ding Q, Li X, Zhao X, et al. Punching pores on cellulose fiber paper as the spacer of triboelectric nanogenerator for monitoring human motion. Energy Reports 2020;6:2851–60. https://doi.org/10.1016/j.egyr.2020.10.011.
[58] Gao S, Yang LH, Gan Y, Chen Q. The Influence of Sliding Speed on the Friction Behavior of Silica Surface. ACS Omega 2021;6:3384–9. https://doi.org/10.1021/acsomega.0c05897.
[59] Zhang C, Zhou T, Tang W, Han C, Zhang L, Wang ZL. Rotating-Disk-Based Direct-Current Triboelectric Nanogenerator. Adv Energy Mater 2014;4:1301798. https://doi.org/10.1002/aenm.201301798.
[60] Chung S-H, Jang YH, Kim D, Lee J, Kim S, Park JY, et al. High-Output Wearable Flow Ring-Based Triboelectric Nanogenerator via Opposite Charging Intermediate Layer. Int J Energy Res 2023;2023:1–8. https://doi.org/10.1155/2023/3415211.
[61] Vu DL, Le CD, Nguyen QT, Ahn KK. Driving the Polyvinylidene Fluoride Crystallization via Surface Functionalization of Ferromagnetic Nanoparticles for Liquid-Solid Triboelectric Nanogenerator Enhancement. Int J Energy Res 2023; 2023:1–11. https://doi.org/10.1155/2023/3702593.
[62] Zhao Z, Dai Y, Liu D, Zhou L, Li S, Wang ZL, et al. Rationally patterned electrode of direct-current triboelectric nanogenerators for ultrahigh effective surface charge density. Nat Commun 2020;11:1–9. https://doi.org/10.1038/s41467-020-20045-y.